Supplementary Information: Elasticity of colloidal gels: structural heterogeneity, floppy modes, and rigidity

D. Zeb Rocklin,[1,2] Lilian C. Hsiao,[3] Megan Szakasits,[4] Michael J. Solomon,[4] and Xiaoming Mao[1]

[1] *Department of Physics, University of Michigan, Ann Arbor, MI 48109*
[2] *School of Physics, Georgia Institute of Technology, Atlanta, GA 30332*
[3] *Department of Chemical and Biomolecular Engineering, North Carolina State University, Raleigh, NC 27695*
[4] *Department of Chemical Engineering, University of Michigan, Ann Arbor, MI 48109*

I. ADDITIONAL INFORMATION ON EXPERIMENTS

A. Sample preparation

We synthesize poly(methyl methacrylate) (PMMA) colloids (radius $a = 0.58\mu m \pm 4\%$) that are sterically stabilized with a 10-nm layer of poly(12-hydroxystearic acid) (PHSA). The colloids are dyed with fluorescent Nile Red and are suspended at various volume fractions ($\phi = 0.15, 0.20, 0.25, 0.30, 0.35$, and 0.40) in a mixture of cyclohexyl bromide (CHB) and decalin (63:37 v/v). Non-adsorbing polystyrene (molecular weight MW = 900,000 g/mol, radius of gyration $R_g = 41$ nm) is added at a dilute concentration ($c/c^* = 0.4$ and 0.5, where c^* is the overlap concentration of the depleting polymer) to induce a short-ranged depletion attraction that leads to gelation. Charge screening is provided by adding 1μM tetrabutylammonium chloride (Debye length = 730 nm, zeta potential ≤ 10 mV) to the gels.

B. Confocal microscopy

An inverted confocal microscope (Nikon A1Rsi) equipped with a resonant scanner head and a high-speed piezo stage is used to capture the 3D structure of the gel microstructure. The image volumes are captured at dimensions of $31\mu m \times 31\mu m \times 25\mu m$ (voxel size = $60nm \times 60nm \times 60nm$) with a lag time of $\Delta t = 0.074s$. Images are obtained from three independent locations within the same sample, at a distance of $\geq 15\mu m$ above the coverslip. Particle centroids are identified using a standard image processing algorithm developed by Crocker and Grier that identifies the local regional maximum of fluorescence intensity in 3D space [1].

C. Rheology

The viscoelasticity of the gel samples are characterized using a stress-controlled rheometer (TA Instruments, AR-G2). Freshly prepared colloidal gels are loaded onto a Peltier plate at $T = 25°C$. A $6cm$ steel parallel plate geometry is lowered to a gap of $300\mu m$ while rotating slowly (angular frequency, $\omega = 0.1$ rad/s) to minimize the formation of bubbles at the interface. A solvent trap filled with CHB and decalin is used to minimize evaporation over the duration of the experiments. The suspensions are presheared at 10 rad/s for 1 minute, then allowed to gel over 30 minutes. The frequency-dependent storage and viscous moduli, $G'(\omega)$ and $G''(\omega)$, are measured for the gels using oscillatory frequency sweep measurements where the applied frequencies are varied from 100 rad/s to 0.1 rad/s at a fixed linear strain of $\lambda = 0.005$.

II. INTERACTION POTENTIAL OF THE COLLOIDAL PARTICLES AND VISCOUS DRAG

The colloidal particles of radius $a = 0.58\mu$m are attracted to one another by the depletion effect of the polymers of radius of gyration $R_g = 41$nm and concentration $c/c^* = 0.4, 0.5$, leading to the Asakura Oosawa potential [2]

$$U_{\mathrm{AO}}(r) = -k_B T \frac{c}{c^*} \frac{1}{R_g^3} \times \left((R_g + a)^3 - \frac{3}{4}(R_g + a)^2 r + \frac{1}{16} r^3 \right), \quad (1)$$

where r is the distance between the centers of the two particles. Additionally, the colloidal particles undergo a screened electrostatic repulsion of the DLVO form that, neglecting the small van der Waals component, takes the form [3]

$$U_{\mathrm{DLVO}}(r) = \frac{k_B T Z^2 \lambda_B}{r(1 + \kappa a)^2} \exp\left[-\kappa(r - 2a)\right], \quad (2)$$

where κ^{-1} is the Debye length (7.3×10^{-7}m) and λ_B the Bjerrum length (1.37×10^{-8}m). $Z = 108.58$ is the magnitude of the effective charge of the colloidal particles in units of the fundamental charge. Including additionally the van der Waals forces does not appreciably alter the spring constants obtained.

The Stokes drag, treating colloidal particles as ideal spheres with no hydrodynamic interactions, is a force opposing the motion of the particles relative to the fluid, of magnitude

$$\mathbf{F}_d = 6\pi a \eta \mathbf{v}, \quad (3)$$

where v is particle velocity and $\eta = 0.0025\,\mathrm{Pa \cdot s}$ is the dynamic viscosity. Considering harmonic motion of the

form $\mathbf{u}(t) = \mathbf{u}e^{i\omega t}$, $\mathbf{F} = -m\omega^2\mathbf{u}, \mathbf{v} = i\omega\mathbf{u}$ (the physical components being the real parts). We neglect the inertial term, which is much smaller than the Stokes term.

III. EFFECTIVE SPRING CONSTANT AT FINITE TEMPERATURE AND FREQUENCY

In this section we derive the effective spring constant between bonded pairs of colloidal particles in the gels. At zero temperature, this would be determined simply by the quadratic term of the expansion about the minimum of the interaction potential between particles shown in Fig. 3(a) in the main text, which would depend largely on the sharpness of the hard-wall repulsion between particles. However, as can be seen in the vertical scale, measured in units of k_BT, thermal fluctuations drive the particles to explore a broad range of separations over which the potential is quite anharmonic. Despite this nonlinearity in the interaction, the *response*, determined by the free energy, is nevertheless linear for sufficiently small forces and strains (actually, in our case even $U(r)$ contains a statistical contribution, since it includes depletion interactions from polymers). Indeed, this is a particular case of the fluctuation-dissipation theorem, in which the linear response of a thermal system is determined entirely by that system's fluctuations and correlations in the absence of external forces. We now illustrate how this is done in this case.

Consider a particle at temperature T subject both to a one-dimensional potential $U(r)$ and a weak external field f so that it experiences an effective potential

$$U_f(r) = U(r) - fr, \tag{4}$$

and the expectations of observables is given by

$$\langle \hat{O}_f(r) \rangle = \frac{\int dr\, \hat{O}_f(r) \exp\left[-U_f(r)/k_BT\right]}{\int dr\, \exp\left[-U_f(r)/k_BT\right]}. \tag{5}$$

Following the paradigm of the fluctuation-dissipation theorem, the effective "spring constant" is simply defined as the ratio of the applied field to the resultant displacement,

$$k_{\text{eff}}^{-1} = \frac{\langle r \rangle|_f - \langle r \rangle|_{f=0}}{f}. \tag{6}$$

We then expand to linear order in the weak field f and obtain the spring constant

$$k_{\text{eff}} = \frac{k_BT}{\langle r^2 \rangle - \langle r \rangle^2}. \tag{7}$$

Note that this calculation is done using a one dimensional potential. Extending it to three dimensions will lead to a geometric factor of $O(1)$, but this correction is negligible for small fluctuations which is the case of our interest.

More generally, because the external force of the rheometer is applied at finite frequency, we could consider finite-time correlations (via Fourier transform) to determine a frequency-dependent spring constant. However, since the thermal equilibration time is short compared to the periods explored in the rheometer, the force experienced is effectively constant in time. Thus, to good approximation $k_{\text{eff}}(\omega) \approx k_{\text{eff}}(0)$, as used in the main text.

This result coincides with that predicted by the equipartition theorem. However, the above approach has the added utility of accounting for nonlinear potentials, demonstrating that the thermal fluctuations root the effective interaction in the long-range features of the electrostatic and depletion interactions rather than the short-range hard-wall repulsion.

IV. CALCULATING FREQUENCY DEPENDENT SHEAR MODULI FROM MICROSTRUCTURES

We obtain positions of particles within the $30.72\mu\text{m} \times 30.72\mu\text{m} \times 25.08\mu\text{m}$ scan window via confocal microscopy. As discussed in the main text, we model the particle dynamics as the following equation of motion

$$\mathbf{F}_i = -k_{\text{eff}} \sum_{\langle i,j \rangle} \hat{\mathbf{r}}_{ij} \left[\hat{\mathbf{r}}_{ij} \cdot (\mathbf{u}_i - \mathbf{u}_j)\right] + 6\pi i\omega\eta_f a \left(\mathbf{u}_i - \mathbf{u}_i^{\text{aff}}\right). \tag{8}$$

Within our scan window, we fix the particles within a single bond length of two opposing sides to undergo uniform shear strain at fixed frequencies. Each type of strain can be written in terms of a deformation gradient Λ such that the affine displacement of each particle $\mathbf{r}_i$ is $\mathbf{u}_i^{\text{aff}} \equiv (\Lambda - I) \cdot \mathbf{r}_i$. Boundary particles are assumed to follow the affine displacements. We can combine these displacements into a single vector of all the boundary displacements, $\mathbf{u}_B$. Internal particles have displacements $\mathbf{u}_I$ which can be nonaffine, such that the total force on each internal particle, as given in Eq. (8), is zero (neglecting the small inertial term). We can use Eq. (8) to relate the forces to the displacements via the following matrix equation.

$$\begin{pmatrix} 0 \\ \mathbf{f}_B \end{pmatrix} = \begin{pmatrix} \mathbf{D}_{II} & \mathbf{D}_{IB} \\ \mathbf{D}_{BI} & \mathbf{D}_{BB} \end{pmatrix} \begin{pmatrix} \mathbf{u}_I \\ \mathbf{u}_B \end{pmatrix} - 6\pi i\omega\eta_f a \begin{pmatrix} \mathbf{u}_I - \mathbf{u}_I^{\text{aff}} \\ 0 \end{pmatrix}, \tag{9}$$

where $\mathbf{D}$ is the dynamical matrix from the first term in Eq. (8) and we have separated it into boundary and inner parts, and drag force is included as a second term. At finite frequencies, this matrix equation is exactly solvable for any given $\mathbf{u}_B$, allowing us to obtain both the nonaffine displacements in the interior $\mathbf{u}_I$ and the forces $\mathbf{f}_B$ on the boundary particles necessary for the shearing motion. At zero frequency, there is a possibility of internal

zero modes, leaving the interior displacements not fully defined but not affecting the boundary forces.

Dividing the total boundary force by the area of the boundary, we find the stress induced by the given shear strain. The real and imaginary parts of the ratio of stress to strain are the storage and loss moduli, $G'(\omega), G''(\omega)$. We average over the components of shear moduli obtained from a full Cartesian basis $(\sigma_{xy}, \sigma_{yz}, \sigma_{zx})$. At low frequencies, the nonaffine displacements approach a well-defined limit, which minimizes elastic energy. This limit is finite for most samples we studied, leading to a low-frequency plateau in $G'(\omega)$, and vanishes only for some low density samples. As frequency increases, each particle experiences an increasing drag force that inhibits nonaffine deformations, so that the deformation becomes increasingly affine. At high frequencies, the displacements achieve the affine limit, again leading to a (much higher) plateau in the storage modulus.

V. FLOPPY-MODES VISUALIZATION

In this section we show some visualization of the floppy modes. Figure 1 shows one example of floppy modes plot for the whole system and zoomed in for a small volume to show the details. Since floppy modes don't change the bond lengths, these displacements simply rotate the bonds.

VI. THE LOSS SHEAR MODULI G''

In this section we include additional figures and discussions concerning the loss shear moduli $G''(\omega)$.

Our microscopic model directly gives a loss shear modulus associated with the gel network, and the $G''(\omega)$ we compare to the experiments is a sum of this network loss modulus and the loss modulus purely coming from the viscosity of the solvent, $\eta_f\omega$.

Figure 2 shows a comparison between measured and calculated (using our microscopic model) $G''(\omega)$. The agreement is qualitative, in terms of the general trend of how G'' changes as a function of ω and control parameters $(\phi, c/c^*)$. The discrepancy is a result of both finite scan window size and hydrodynamic effect which is ignored in our model.

Figure 3 shows some additional figures where experimental and theory results for G' and G'' are shown on the same plot.

VII. PHENOMENOLOGICAL SPRING-DASHPOT MODEL PARAMETERS

In this section we discuss parameters used in the phenomenological spring-dashpot model collapse of our data, including the affine and nonaffine shear modulus $G_{\rm A}, G_{\rm NA}$, and the coupling viscosity between the affine shear modulus and the viscous dashpot η_c. The fluid viscosity is $\eta_f = 0.0025$ Pa·s for all samples, same as used in the microscopic model.

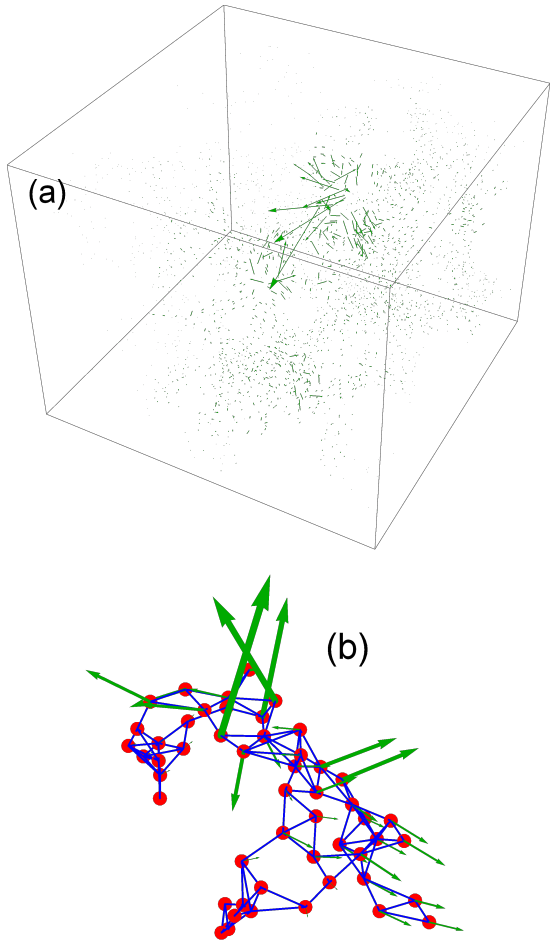

FIG. 1. A particular nearly zero-energy mode is shown for a $\phi = 0.15, c/c^* = 0.4$ sample is shown. In (a), each green arrow begins at the center of a colloidal particle, with the arrow's magnitude and direction depicting that of the displacement vector of the mode. In (b), a small region of the scan is shown, with the centers of particles represented as red dots with blue lines connecting particles in contact.

A. Affine limit of shear moduli

In this subsection we derive the affine limit of shear moduli $G_{\rm A}$ [Eq.(6) in main text]. Without loss of generality we assume a simple strain with a displacement gradient tensor

$$\Lambda = \begin{pmatrix} 1 & 0 & \gamma \\ 0 & 1 & 0 \\ 0 & 0 & 1 \end{pmatrix}, \tag{10}$$

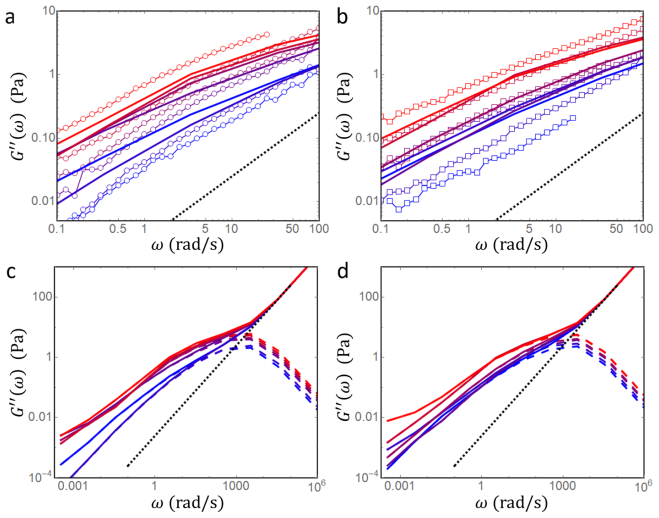

FIG. 2. (a-b) Experimental (open symbols) and model (curves, same color of symbol and curve correspond to the same parameters) values of $G''(\omega)$ at $c/c^* = 0.4$ (a) and $c/c^* = 0.5$ (b) for different values of ϕ. Colors and symbols are the same as in Fig. 2 in the main text. The black dotted line shows the solvent contribution, $\eta_f\omega$, which is already included in the curves. (c-d) Model values of G'' in a wider frequency window, showing the crossover. Solid and long-dashed curves are G'' with and without the solvent contribution, and the black dotted line shows the solvent contribution, $\eta_f\omega$. The pure network part (long-dashed curves) is well captured by the phenomenological spring-dashpot model as shown in Fig. 4b in the main text.

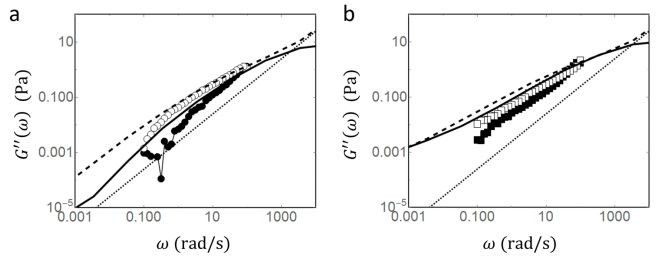

FIG. 3. Storage (G', solid circles) and loss (G'', open circles) shear moduli from rheological measurements (data points, black for G' and white for G'') and computation (curves, solid for G' and long-dashed for G''). The solvent contribution to G'' is shown as a dotted line. (a) shows data at $\phi = 0.2, c/c^* = 0.4$ and (b) shows data at $\phi = 0.2, c/c^* = 0.5$.

and the resulting elastic energy in volume V is

$$E = \frac{1}{2}GV\gamma^2, \tag{11}$$

where G is the shear modulus.

Next we consider this elastic energy as coming from stretching bonds between colloidal particles and obtain a simple estimate for G in the affine limit. The total number of bonds in volume V for a colloidal gel with volume fraction ϕ and mean coordination number z is given by

$$N_{\rm bonds} = \frac{V\phi(z/2)}{(4/3)\pi a^3}, \tag{12}$$

where a is the particle radius. The elastic energy of one bond (of length $2a$) in direction (θ, ψ) in polar coordinate, under the affine strain in Eq. (10) is

$$E_1 = 2k_{\rm eff}\, a^2\gamma^2 \cos^2\theta \sin^2\theta \cos^2\psi. \tag{13}$$

Averaging over all solid angles we find

$$\langle E_1\rangle = \frac{2}{15}k_{\rm eff}\, a^2\gamma^2. \tag{14}$$

The total elastic energy in volume V is then the contribution of all bonds,

$$E = N_{\rm bonds}\langle E_1\rangle. \tag{15}$$

Equaling the above quantity with the continuum elasticity expression (11) we find the affine shear moduli

$$G_{\rm A} \simeq \frac{\phi\langle z\rangle k_{eff}}{10\pi a}, \tag{16}$$

which is Eq.(5) in main text.

B. List of parameters in phenomenological spring-dashpot model

In this subsection we list all parameters we used in the data collapse shown in Fig. 4(c-d) in the main text: $G_{\rm A}$ obtained using Eq. (6) in the main text, $G_{\rm NA}$ obtained by averaging over $G'(\omega)$ for $\omega < 0.2$ rad/s, η_c obtained by fitting $G''(\omega) - \eta_f\omega$ as a straight line $\eta_c\omega$ for $\omega < 1$ rad/s (see discussions below Eq.(6) in the main text). Fluid viscosity $\eta_f = 0.0025$ Pa.s for all samples.

We also plot $G_{\rm NA}$ as a function of ϕ in Fig. 4, and compare it with a power law with exponent 5.

ϕ	0.15	0.2	0.25	0.3	0.35	0.4
$G_{\rm A}$(Pa)	5.27	7.03	8.79	10.54	12.30	14.06
$G_{\rm NA}$(Pa)	0.0010	0.0005	0.0125	0.0073	0.0485	0.0758
η_c(Pa · s)	0.042	0.053	0.151	0.232	0.372	1.040

TABLE I. Phenomenological spring-dashpot model parameters for the case of $c/c^* = 0.4$.

ϕ	0.15	0.2	0.25	0.3	0.35	0.4
$G_{\rm A}$(Pa)	10.31	13.75	17.19	20.63	24.06	27.50
$G_{\rm NA}$(Pa)	0.0022	0.0047	0.0242	0.0328	0.1279	0.3279
η_c(Pa · s)	0.042	0.078	0.276	0.271	0.597	1.113

TABLE II. Phenomenological spring-dashpot model parameters for the case of $c/c^* = 0.5$.

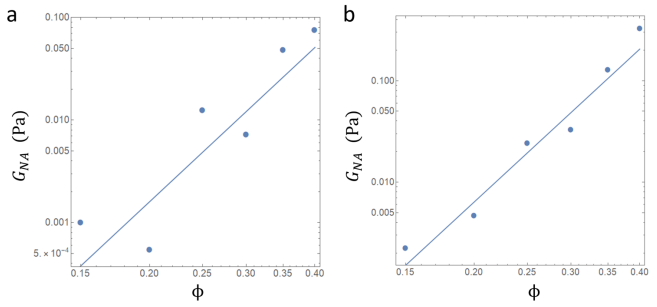

FIG. 4. Nonaffine shear modulus G_{NA} as a function as ϕ for $c/c^* = 0.4$ (a) and $c/c^* = 0.5$ (b). The lines show a power law relation with exponent 5.

[1] J. C. Crocker and D. G. Grier, Journal of colloid and interface science **179**, 298 (1996).

[2] S. Asakura and F. Oosawa, Journal of Polymer Science Part A: Polymer Chemistry **33**, 183 (1958).

[3] E. J. W. Verwey, J. T. G. Overbeek, and J. T. G. Overbeek, *Theory of the stability of lyophobic colloids* (Courier Corporation, 1999).